Surface instabilities of soft dielectric elastomers with implementation of electrode stiffness

Pietro Liguori[1], Massimiliano Gei[2]

[1] *School of Engineering, Cardiff University, The Parade, Cardiff CF24 3AA, Wales, U.K.*
[2] *Department of Engineering and Architecture, University of Trieste,*
via A. Valerio 6/1, 34127 Trieste, Italy
Email: LiguoriP@cardiff.ac.uk, massimiliano.gei@dia.units.it

February 14, 2022

Abstract

This paper contains a thorough investigation into plane-strain electro-elastic surface instabilities of dielectric elastomers. We employ a systematic approach to our investigation, introducing three ways to actuate an elastomer device, namely, actuation by means of (i) attached compliant electrodes, (ii) sprayed charges onto the opposite surfaces and (iii) fixed electrodes between which the device 'floats' in vacuum and expands transversally. We examine electro-mechanical instability with particular attention to the third listed mode of actuation and the features of the specimen. We then tackle surface instability for the three modes, showing the relationship between applied pre-stress and the stability domain, as well as the characteristics of the obtained bifurcation fields. The effects of the stiffness of the electrode (relevant in the first listed mode of actuation) on surface instabilities are then investigated, by adopting an elastic surface-substrate interaction model in which the properties of the coating enters in the boundary conditions for the substrate. Various electrode materials are assumed, demonstrating that their implementation in the model increases the number of solutions at bifurcation and changes the overall stability domain. We present this new enriched bifurcation map, showing the dependence on the wavenumber, and characterise the solutions by examining the bifurcated fields.

1 Introduction

Dielectric elastomer actuators (DEAs) typically consist of an elastomer membrane actuated by a difference in electric potential across the thickness, which induces in-plane large strains. They have attracted interest in areas such as soft robotics [1, 2, 3], mechanical [4, 5, 6], biomedical [7, 8, 9] and energy engineering [10, 11, 12, 13] (the review [14] provides a broad overview of the topic).

The classic configuration for these actuators (first reported by Pelrine et al. [15]) consists of a film sandwiched between compliant electrodes (carbon grease, ion-implanted polymers, ionogels, etc.). Spraying charges directly on the surface of the elastomer is another way to actuate a dielectric elastomer film. This method was pioneered by Röntgen [16] and proposed recently by Keplinger et al. [17] who showed experimentally how surface charges could be sprayed onto the elastomer. A third possible actuation mode is that where the membrane 'floats' between two fixed electrodes surrounded by either a fluid or a vacuum. This was proposed by Díaz-Calleja et al. [18] who addressed nonlinear actuation law and pull-in instability in terms of contrast between dielectric permittivities of the elastomer and surrounding environment.

DEAs exhibit a wide variety of failure modes making their optimisation and implementation difficult. While, on the one hand, electric breakdown is the main limitation due to intrinsic material properties [19, 20], on the other hand, failures associated with electro-mechanical instability [21, 22], localised bifurcations [23, 24, 25] and diffuse-mode bifurcations [26] play a major role, the latter being particularly promoted by the slenderness of the typical devices. Among diffuse-mode bifurcations, surface instability provides important indications regarding the limit of short-wavelength mode. For an electro-elastic half-space, Dorfmann and Ogden [27] present the relevant framework by using the theory of linearised incremental deformations and electric fields superimposed on a known underlying configuration, to study a half-space actuated by compliant electrodes in plane strain.

In this paper, we undertake a systematic approach to investigate surface bifurcations of electro-elastic half-spaces deforming homogeneously in the fundamental path according to the three actuation modes introduced earlier, i.e., voltage-actuated, charge-actuated and voltage-actuated 'floating' specimen. The large strain relationships for all paths are laid out by adopting both neo-Hookean and Gent electro-elastic constitutive models; particular attention is devoted to the less-studied 'floating' actuator surrounded by vacuum for which conditions for electro-mechanical instability and 'expansion limit' are provided.

The effect of the stiffness of electrodes is commonly neglected in electro-elastic actuation as they are assumed to be fully compliant. Elastic surface-substrate interactions, a valid model for thin, stiff films coating elastic solids, were analysed by Murdoch [28] and later by Ogden and Steigmann [29, 30] whom refined the theory and introduced the bending stiffness. The latter approach is used here to take into account the effects of the electrode on surface bifurcations of half-spaces that are deformed controlling the voltage. Guided by experimental measurements, three different kinds of electrodes are analysed possessing a range of material parameters to cover a variety of cases and assess their

effects on electro-elastic surface instability and bifurcation modes. The results show that they may limit considerably the stability domain when the half-space contracts.

2 Large deformations and stress state in a soft dielectric body

In this section, the general theory of large-strain electro-elasticity for a homogeneous isotropic materials is introduced. This will include general kinematics and constitutive equations which describe the electro-mechanical response of the material.

2.1 Kinematics and field equations

We assume that in the stress-free configuration the electro-elastic material occupies a region $B^0 \in \mathbb{R}^3$. After a given deformation $\boldsymbol{\chi}$, the deformed body covers a space $B \in \mathbb{R}^3$. We can define a material particle in B^0 by its position vector $\boldsymbol{x}^0$ that is transformed to $\boldsymbol{x} = \boldsymbol{\chi}(\boldsymbol{x}^0)$ in B; $\boldsymbol{F} = \partial\boldsymbol{\chi}/\partial\boldsymbol{x}^0$ denotes the deformation gradient. The space surrounding the body will be denoted by B^{sur} with the particular case of vacuum being denoted by B^*.

In the deformed configuration B, we assume that the total stress is denoted by $\boldsymbol{\tau}$ while electric and displacement fields are indicated with $\boldsymbol{E}$ and $\boldsymbol{D}$, respectively. Under the assumption of the absence of both volume free charges and body forces, the governing equations are the following:

$$\mathrm{div}\,\boldsymbol{\tau} = \boldsymbol{0}, \quad \boldsymbol{\tau}^T = \boldsymbol{\tau}, \quad \mathrm{div}\,\boldsymbol{D} = 0, \quad \mathrm{curl}\,\boldsymbol{E} = \boldsymbol{0}. \tag{2.1}$$

The last equation implies that $\boldsymbol{E}$ can be derived from the electric potential $\phi(\boldsymbol{x})$ such that $\boldsymbol{E} = -\mathrm{grad}\phi(\boldsymbol{x})$. In vacuum, eqs. (2.1) specialise to

$$\mathrm{div}\,\boldsymbol{T}^* = \boldsymbol{0}, \quad \boldsymbol{T}^* = (\boldsymbol{T}^*)^T, \quad \mathrm{div}\,\boldsymbol{D}^* = 0, \quad \mathrm{curl}\,\boldsymbol{E}^* = \boldsymbol{0}, \tag{2.2}$$

where $\boldsymbol{T}^*$ is the Maxwell stress, i.e.

$$\boldsymbol{T}^* = \varepsilon_0\Big(\boldsymbol{E}^* \otimes \boldsymbol{E}^* - \frac{1}{2}(\boldsymbol{E}^* \cdot \boldsymbol{E}^*)\boldsymbol{I}\Big). \tag{2.3}$$

In eq. (2.3), $\varepsilon_0 = 8.85 \cdot 10^{-12}\,\mathrm{Fm}^{-1}$ is the permittivity of the vacuum and $\boldsymbol{I}$ is the appropriate identity tensor. The electric quantities follow the relationship $\boldsymbol{D}^* = \varepsilon_0\boldsymbol{E}^*$, while eq. $(2.2)_4$ implies $\boldsymbol{E}^* = -\mathrm{grad}\phi^*(\boldsymbol{x})$.

In the deformed configuration, we can define jump conditions at the boundaries across a surface discontinuity,

$$\boldsymbol{n} \cdot [\![\boldsymbol{D}]\!] = -\omega, \quad \boldsymbol{n} \times [\![\boldsymbol{E}]\!] = \boldsymbol{0}, \quad [\![\boldsymbol{\tau}]\!]\boldsymbol{n} = \boldsymbol{t}, \tag{2.4}$$

where the brackets $[\![\,]\!]$ indicate a 'jump' in the quantity concerned across the surface, defined as $[\![\cdot]\!] = (\cdot)_B - (\cdot)_{B^{sur}}$. Here, $\boldsymbol{n}$ is the outward unit normal to B, ω is the surface

charge density and t is the mechanical traction. When the discontinuity occurs at the boundary between the elastomer and an adjacent vacuum the above equations specialise as

$$\boldsymbol{n} \cdot \boldsymbol{D} = -\omega + \varepsilon_0 \boldsymbol{E}^* \cdot \boldsymbol{n}, \quad \boldsymbol{n} \times (\boldsymbol{E} - \boldsymbol{E}^*) = \boldsymbol{0}, \quad \boldsymbol{\tau} \boldsymbol{n} = \boldsymbol{t} + \boldsymbol{T}^* \boldsymbol{n}. \tag{2.5}$$

It could be useful to define nominal or Lagrangian measures. Following the usual argument, the total first Piola-Kirchhoff stress tensor is defined as a two-point tensor as

$$\boldsymbol{S} = J \boldsymbol{\tau} \boldsymbol{F}^{-T}, \tag{2.6}$$

where $J = \det \boldsymbol{F}$, while the Lagrangian electric displacement and electric fields are given by

$$\boldsymbol{D}^0 = J \boldsymbol{F}^{-1} \boldsymbol{D}, \quad \boldsymbol{E}^0 = \boldsymbol{F}^T \boldsymbol{E}, \tag{2.7}$$

respectively. The governing eqs. (2.1) updated to the reference configuration thus become:

$$\mathrm{Div} \boldsymbol{S} = \boldsymbol{0}, \quad \boldsymbol{S} \boldsymbol{F}^T = \boldsymbol{F} \boldsymbol{S}^T, \quad \mathrm{Div} \boldsymbol{D}^0 = 0, \quad \mathrm{Curl} \boldsymbol{E}^0 = \boldsymbol{0}, \tag{2.8}$$

where differentiation is taken now with respect to coordinates in B^0.

2.2 Electro-elastic constitutive equations

The material considered in the analysis can be defined by an electro-elastic strain-energy function W which is based on the deformation gradient and nominal electrical displacement $\boldsymbol{D}^0$ such that $W = W(\boldsymbol{F}, \boldsymbol{D}^0)$. Throughout the paper the material is assumed to be incompressible such that $J = 1$. For such a material, the constitutive equations take the form

$$\boldsymbol{S} = \frac{\partial W}{\partial \boldsymbol{F}} - p \boldsymbol{F}^{-T}, \quad \boldsymbol{E}^0 = \frac{\partial W}{\partial \boldsymbol{D}^0}, \tag{2.9}$$

where p represents an unknown hydrostatic pressure to be defined by boundary conditions. Isotropy requires that $W(\boldsymbol{F}, \boldsymbol{D}^0)$ be a function of both the invariants of the right Cauchy-Green tensor $\boldsymbol{C} = \boldsymbol{F}^T \boldsymbol{F}$, namely

$$I_1 = \mathrm{tr} \boldsymbol{C}, \quad I_2 = \frac{1}{2} \Big[(\mathrm{tr} \boldsymbol{C})^2 - \mathrm{tr}(\boldsymbol{C}^2) \Big], \quad I_3 = \det \boldsymbol{C} = 1, \tag{2.10}$$

and those involving both $\boldsymbol{C}$ and $\boldsymbol{D}^0$, i.e.

$$I_4 = \boldsymbol{D}^0 \cdot \boldsymbol{D}^0, \quad I_5 = \boldsymbol{D}^0 \cdot \boldsymbol{C} \boldsymbol{D}^0, \quad I_6 = \boldsymbol{D}^0 \cdot \boldsymbol{C}^2 \boldsymbol{D}^0. \tag{2.11}$$

It is to note that a convenient form of the energy function $W(I_i)$ ($i = 1, \dots, 6$) is the one where the purely elastic part is split from the remaining part involving coupled electrostatic effects, namely $W(I_i) = W_{elas}(I_1, I_2) + W_{elec}(I_4, I_5, I_6)$.

For the elastic part, two models are employed: the first one is the simple neo-Hookean solid, defined as

$$W_{elas}(I_1) = \frac{\mu}{2}(I_1 - 3), \tag{2.12}$$

where μ is the shear modulus of the material; the second one is the Gent material model, whose energy is given by

$$W_{elas}(I_1) = -\frac{\mu J_m}{2} \mathrm{Ln}\left(1 - \frac{I_1 - 3}{J_m}\right). \tag{2.13}$$

The latter model is better suited for rubber-like material at large strains as it incorporates the idea of a limit stretch as the polymer chains extend fully. This limit is defined by the Gent parameter $J_m = I_1^{lim} - 3$ where I_1^{lim} is the first invariant evaluated at the stretch limit value. As $J_m \to \infty$, the neo-Hookean model is obtained.

Our goal is to investigate electro-elastic problems where the material behaves as an ideal dielectric, i.e. the permittivity ε is independent of the strain. This behaviour can be captured by a function $W_{elec}(I_5)$ in which the coefficient in front of the invariant is constant. However, for some reasons that will be described later, we introduce the expression of W_{elec} proposed by Gei et al. [31] that depends on all the three invariants I_4, I_5, I_6, namely

$$W_{elec} = \frac{1}{2\varepsilon}(\bar{\gamma}_0 I_4 + \bar{\gamma}_1 I_5 + \bar{\gamma}_2 I_6), \tag{2.14}$$

where ε is to be read as the permittivity of the material in the natural configuration and $\bar{\gamma}_i$ $(i = 0, 1, 2)$ are dimensionless constants such that $\sum_i \bar{\gamma}_i = 1$. As $\bar{\gamma}_0, \bar{\gamma}_2 \to 0$ (and then $\bar{\gamma}_1 \to 1$), the energy function becomes that of an ideal dielectric where the permittivity is independent of the current strain for which, through eq. $(2.9)_2$ and eqs. (2.7), the relationship between $\boldsymbol{E}$ and $\boldsymbol{D}$ becomes

$$\boldsymbol{D} = \varepsilon\boldsymbol{E}. \tag{2.15}$$

2.3 Linearized incremental deformation formulation

This section summarizes the linear incremental deformation theory that allows for the study of the onset of diffuse and localised bifurcation modes, referring to Bertoldi and Gei [22] and Dorfmann and Ogden [27] for more details. This method will then be specialised for the electro-elastic surface instability problems addressed later on.

The way the method works is by superimposing incremental deformations upon a given configuration. A perturbation of nominal surface charges and tractions applied on the boundary of B^0, namely $\dot{\omega}^0$ and $\dot{\boldsymbol{t}}^0$, respectively, is considered such that a new equilibrium configuration is reached where eqs. (2.4) and (2.8) are satisfied. The incremental displacement and deformation gradient are defined similarly to the finite counterpart as $\dot{\boldsymbol{x}} = \dot{\boldsymbol{\chi}}(\boldsymbol{x}^0)$ and $\dot{\boldsymbol{F}} = \mathrm{Grad}\dot{\boldsymbol{\chi}}$, respectively, where onwards a superposed dot ($\dot{\ }$) represents the increment in the quantity concerned. In the current framework, the governing eqs. (2.8) turn into the following

$$\mathrm{Div}\dot{\boldsymbol{S}} = \boldsymbol{0}, \quad \mathrm{Div}\dot{\boldsymbol{D}}^0 = 0, \quad \mathrm{Curl}\dot{\boldsymbol{E}}^0 = \boldsymbol{0}. \tag{2.16}$$

The constitutive eqs. (2.9) can be linearised provided that all incremental quantities are small, as:

$$\dot{S}_{iJ} = -\dot{p}F_{Ji}^{-1} + pF_{Li}^{-1}\dot{F}_{kL}F_{Jk}^{-1} + C_{iJkL}^0\dot{F}_{kL} + B_{iJM}^0\dot{D}_M^0,$$
$$\dot{E}_M^0 = B_{iJM}^0\dot{F}_{iJ} + A_{MN}^0\dot{D}_N^0, \tag{2.17}$$

where $\dot{p}$ is an incremental hydrostatic pressure. The components of the relevant tensor appearing in eqs. (2.17) are highlighted to facilitate the understanding between the different quantities. The electro-elastic moduli tensors $\mathbb{C}^0$, $\mathbb{B}^0$, $\mathbb{A}^0$ can be expressed in terms of the strain energy as

$$C_{iJkL}^0 = \frac{\partial^2 W}{\partial F_{iJ}\partial F_{kL}}, \quad B_{iJM}^0 = \frac{\partial^2 W}{\partial F_{iJ}\partial D_M^0}, \quad A_{MN}^0 = \frac{\partial^2 W}{\partial D_M^0\partial D_N^0}, \tag{2.18}$$

which imply the following symmetries

$$C_{iJkL}^0 = C_{kLiJ}^0, \quad A_{MN}^0 = A_{NM}^0.$$

The Lagrangian formulation implied by eqs. (2.16) can be turned into an updated Lagrangian one by using push-forward operations based on the new quantities

$$\boldsymbol{\Sigma} = \dot{\boldsymbol{S}}\boldsymbol{F}^T, \quad \hat{\boldsymbol{D}} = \boldsymbol{F}\dot{\boldsymbol{D}}^0, \quad \hat{\boldsymbol{E}} = \boldsymbol{F}^{-T}\dot{\boldsymbol{E}}^0. \tag{2.19}$$

As a consequence, the updated governing equations take the form

$$\text{div}\boldsymbol{\Sigma} = \boldsymbol{0}, \quad \text{div}\hat{\boldsymbol{D}} = 0, \quad \text{curl}\hat{\boldsymbol{E}} = \boldsymbol{0}. \tag{2.20}$$

The corresponding incremental boundary conditions can be derived from the boundary conditions given in eqs. (2.4) assuming $\boldsymbol{u}(\boldsymbol{x}) = \dot{\boldsymbol{x}}$. In the updated Lagrangian formulation, they are

$$[\![\boldsymbol{u}^0]\!] = \boldsymbol{0}, \quad [\![\boldsymbol{\Sigma}]\!]\boldsymbol{n}dA = \dot{\boldsymbol{t}}^0 dA^0, \quad [\![\hat{\boldsymbol{D}}]\!]\cdot\boldsymbol{n}dA = -\dot{\omega}^0 dA^0, \quad \boldsymbol{n}\times[\![\hat{\boldsymbol{E}}]\!] = \boldsymbol{0}. \tag{2.21}$$

The boundary conditions can be specialised, analogous to eqs. (2.5), when the discontinuity is adjacent to a vacuum as follows:

$$\boldsymbol{\Sigma}\boldsymbol{n}dA = \dot{\boldsymbol{t}}^0 dA^0 + \boldsymbol{\Sigma}^*\boldsymbol{n}dA, \quad \hat{\boldsymbol{D}}\cdot\boldsymbol{n}dA = -\dot{\omega}^0 dA^0 + \hat{\boldsymbol{D}}^*\cdot\boldsymbol{n}dA, \tag{2.22}$$

where

$$\boldsymbol{\Sigma}^* = \dot{\boldsymbol{T}}^* + \boldsymbol{T}^*(\text{tr}[\boldsymbol{L}]\boldsymbol{I} - \boldsymbol{L}^T), \quad \hat{\boldsymbol{D}}^* = \varepsilon_0(\dot{\boldsymbol{E}}^* + (\text{tr}[\boldsymbol{L}]\boldsymbol{I} - \boldsymbol{L})\boldsymbol{E}^*). \tag{2.23}$$

The constitutive equations can be updated through $\boldsymbol{L} = \text{grad}\boldsymbol{u}$, to yield

$$\Sigma_{ir} = C_{irks}L_{ks} + pL_{ri} - \dot{p}\delta_{ir} + B_{irk}\hat{D}_k,$$
$$\hat{E}_i = B_{kri}L_{kr} + A_{ik}\hat{D}_k, \tag{2.24}$$

where δ_{ij} is the Kronecker delta and the updated electro-elastic moduli become

$$C_{irks} = C_{iJkL}^0 F_{rJ}F_{sL}, \quad B_{irk} = B_{iJM}^0 F_{rJ}F_{Mk}^{-1}, \quad A_{ik} = A_{JM}^0 F_{Ji}^{-1}F_{Mk}^{-1}, \tag{2.25}$$

with symmetries applying as before.

2.4 Three electro-elastic problems for a thin elastomer

Throughout the paper, for the same thin elastomer, three electro-elastic problems are investigated, differing from each other by the type of the imposed electric actuation. They are sketched in Fig. 1, which shows the three devices in the deformed configurations. In all cases, the coordinate x_1 singles out the longitudinal axis of the actuator, x_2 is directed across the thickness whereas x_3 is the out-of-plane axis. The material is an ideal dielectric and is assumed to be incompressible. The first problem (Fig. 1 (a)) is the classical one where two perfectly compliant electrodes are attached to the two opposite sides of the membrane [15]. In the second one, Fig. 1 (b), charges are applied directly (typically sprayed) on the surfaces of the material without the use of electrodes [17], a method that was first studied experimentally by Röntgen in 1880 [16]. The third and final problem, Fig. 1 (c), consists of the elastomer deforming (and *floating*) in vacuum between two electrodes held at a fixed distance L, as first studied by Diaz-Calleja et al. [18] (the vacuum can be also substituted by an ideal fluid, in that case the permittivity should be adjusted). Su et al. [32] also examined the instability of a dielectric slab floating in a conductive fluid undergoing equi-biaxial deformation.

In all cases, the elastomer is deformed homogeneously in plane-strain conditions from a thickness d_0 to d (fringing effects are neglected), therefore $d = \lambda_2 d_0 = \lambda_1^{-1} d_0$. The electric field has only the transverse component, therefore $\boldsymbol{E} = [0, E_2, 0]$. A relationship between the potential difference Φ across the device and E_2 can be derived from the fact that in piecewise problems, like those addressed here, the latter is the change in voltage over a given distance. In addition, a (current) pre-stress τ_{pre} could be applied on the deformed configuration along axis x_1. The finite electro-elastic actuation laws of the three problems are summarised below for the neo-Hookean strain-energy. It is understood that a similar procedure can be followed for the Gent material.

2.4.1 A) Attached compliant electrodes

For the first problem, the electric field outside the elastomer vanishes and the potential difference across the electrodes is simply

$$\Phi = E_2 d, \tag{2.26}$$

or, in terms of d_0, and knowing that $D_2 = \varepsilon E_2$ (eq. (2.15)),

$$\Phi = \frac{d_0 D_2}{\varepsilon \lambda_1}. \tag{2.27}$$

The neo-Hookean strain-energy function (2.12) is used in eqs. (2.9) and (2.6) to obtain the total stress $\boldsymbol{\tau}$. The boundary conditions are specialised for the case where no electric field is present on the two outer sides of the film; $\tau_{22} = 0$ is used to solve the pressure term p, and $\tau_{11} = \tau_{pre}$ is employed to obtain the variable D_2. We can hence obtain the relation for Φ in terms of λ_1 given as

$$\Phi = \frac{d_0 \sqrt{\varepsilon^{-1}((\lambda_1^4 - 1)\mu - \tau_{pre}\lambda_1^2)}}{\lambda_1^2}. \tag{2.28}$$
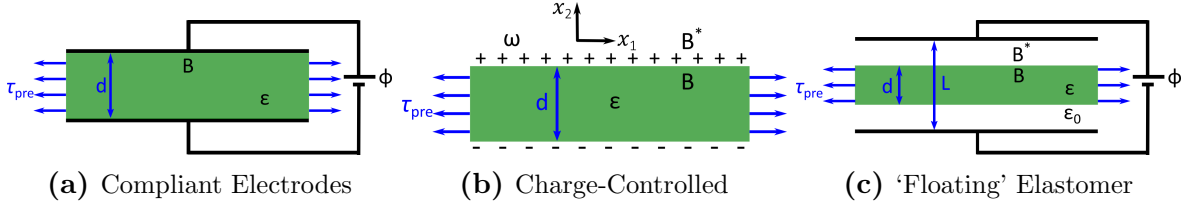
Figure 1: Diagram of the three electro-elastic devices analysed in the paper. d is the thickness of the deformed elastomer, ε the permittivity of the material, L the distance between electrodes and ε_0 the permittivity of the vacuum. The signs in b) indicate the type of charges applied directly to the surface of the elastomer for the charge-controlled case. A pre-stress τ_{pre} is possibly applied to the elastomer.

2.4.2 B) Charge-controlled actuation

When actuation is controlled by the amount of surface charges, whose nominal density is denoted by $\pm\omega_0$, the current longitudinal stretch can be obtained by noting that the jump in the electric displacement, eq. $(2.4)_1$, specialises now to $D_2 = \omega$. Therefore, for the neo-Hookean strain energy, it turns out that

$$\omega = \sqrt{\varepsilon((\lambda_1^2 - \lambda_1^{-2})\mu - \tau_{pre})}. \tag{2.29}$$

It is worth to point out that due to the connection between electric field and electric displacement field, the relationship between Φ and λ_1 coincides with that in eq. (2.28).

2.4.3 C) 'Floating' elastomer in vacuum

In the third problem, the electric potential difference across the fixed electrodes is given by

$$\Phi = E_2^*(L - d) + E_2 d, \tag{2.30}$$

where E_2^* is the only non-vanishing component of the electric field in the vacuum. As the interface between vacuum and elastomer is free from surface charges, from eq. (2.4) we know that $\boldsymbol{D}$ is continuous across this interface and hence $D_2^* = D_2$, revealing that the electric displacement field is constant in the space between electrodes. This leads to the equality $\varepsilon_0 E_2^* = \varepsilon E_2$, which helps to achieve an expression for Φ in terms of E_2 as follows,

$$\Phi = \frac{E_2}{\varepsilon_0}((L - d)\varepsilon + d\varepsilon_0) = \frac{E_2}{\varepsilon_0}((L - d_0\lambda_1^{-1})\varepsilon + d_0\lambda_1^{-1}\varepsilon_0). \tag{2.31}$$

Equivalently, using eq. (2.15), eq. $(2.31)_2$ can be expressed in terms of electric displacement D_2, i.e.

$$\Phi = \frac{D_2}{\varepsilon_0\varepsilon}\left((L - d_0\lambda_1^{-1})\varepsilon + d_0\lambda_1^{-1}\varepsilon_0\right). \tag{2.32}$$

The neo-Hookean strain energy is used in eqs. (2.9) and (2.6) to obtain the total stress $\boldsymbol{\tau}$. The boundary conditions are specialised for the case where a vacuum is in the surrounding space and the Maxwell stress is present; $\tau_{22} = T_{22}^*$ determines the pressure term p, and
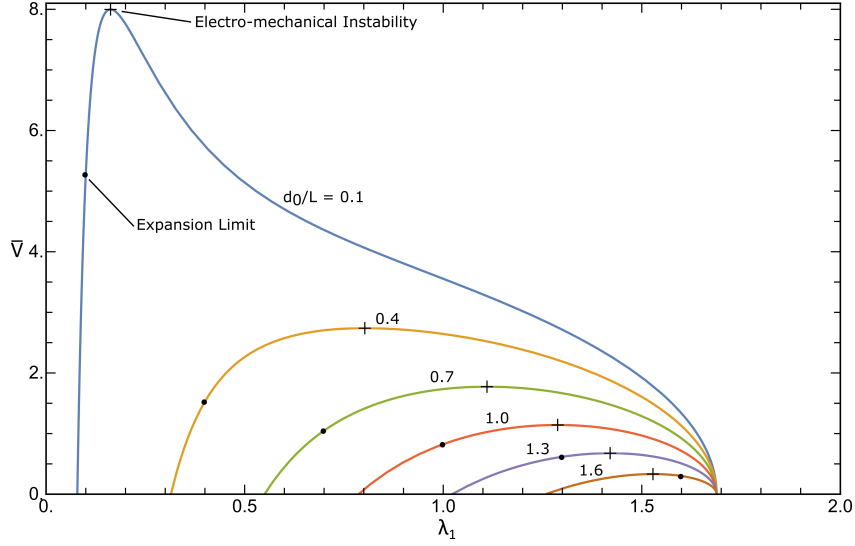
Figure 2: Fundamental loading paths for the actuated 'floating' elastomer in vacuum (neo-Hookean strain energy) with non-dimensional pre-stress $\tau_{pre}/\mu = 2.5$ (various values of the geometric ratio d_0/L are considered). λ_1 varies with the non-dimensional electric potential jump $\bar{V}$. Dots mark the expansion limit, while crosses indicate the onset of the electro-mechanical instability.

$\tau_{11} = \tau_{pre} + T_{11}^*$ yields the electric displacement field D_2. We can hence obtain the relation for Φ in terms of λ_1 given as

$$\Phi = \frac{(d_0(\varepsilon_0 - \varepsilon) + L\varepsilon\lambda_1)\sqrt{(\lambda_1^4 - 1)\mu - \tau_{pre}\lambda_1^2}}{\lambda_1^2\sqrt{\varepsilon\varepsilon_0^2 - \varepsilon^2\varepsilon_0}}. \tag{2.33}$$

An equation for the electro-mechanical instability can be obtained by setting $d\Phi/d\lambda_1 = 0$. This gives the following polynomial

$$L\varepsilon\lambda_1\mu(1 + \lambda_1^4) - d_0(\varepsilon - \varepsilon_0)(\tau_{pre}\lambda_1^2 + 2\mu) = 0, \tag{2.34}$$

where the positive real root corresponds to the onset of electro-mechanical instability.

2.4.4 Analysis of the electro-elastic response of the actuated 'floating' elastomer in vacuum

The fundamental path of the actuated 'floating' elastomer depends on the geometry of the device in the initial configuration. Therefore, we can define a geometrical ratio d_0/L whereby changing it we can obtain different electro-mechanical loading curves. In the floating elastomer configuration, opposite to the charge-controlled and attached compliant electrodes configurations, the elastomer contracts longitudinally and expands transversly, attracted by the fixed electrodes.

Figure 2 shows the loading paths for a neo-Hookean strain energy with an elastomer pre-stressed such that $\tau_{pre}/\mu = 2.5$. In the figure the dimensionless electric potential difference $\bar{V} = (\Phi/L)\sqrt{(\varepsilon/\mu)}$ is reported against the longitudinal stretch λ_1. The black

8

dots represent the threshold beyond which the elastomer expands more than the distance L between the electrodes, hereafter called *expansion limit.* The black crosses show where electro-mechanical instability triggers. Using such a setup, an elastomer with a $d_0/L > 1$ is pre-stressed, causing a transversal contraction and allowing the elastomer to be placed between the fixed electrodes. For large values of d_0/L (e.g. 1.6 in the figure), the elastomer does not exhibit electro-mechanical instability before reaching the 'expansion limit'. In contrast, for $d_0/L \lessapprox 1.491$ the elastomer has enough space to expand and the electro-mechanical instability, analytically predicted by a positive real solution of eq. (2.34), becomes critical. The condition $\Phi = 0$ provides the points where the electro-elastic curve intersects the horizontal axis. Eq. (2.32) yields two solutions, namely

$$D_2 = 0, \quad \frac{d}{L} = \frac{\varepsilon/\varepsilon_0}{\varepsilon/\varepsilon_0 - 1}. \tag{2.35}$$

The former is a trivial solution, i.e. null electric actuation; the latter denotes a configuration not physically meaningful, as the left-hand side must be less than one (equal to one at the expansion limit), while the right-hand side has to be greater than one, as any material will always have a permittivity higher than that of the surrounding vacuum. The expansion of the elastomer will always be limited by the electrodes before this solution can be reached (i.e. the black dot in the figure). Compared to the case with $\tau_{pre} = 0$, not reported in a figure, in a pre-stressed elastomer, the expansion limit appears much later along the curve. The pre-stressed elastomer also allows for higher voltages to be reached before electro-mechanical instability occurs.

Figure 3 shows the loading paths using the Gent strain energy eqs. (2.14) and (2.13). We define λ_{lim} from eq. (2.13) as the limiting stretch under plane-strain conditions. In this case we specialise I_1^{lim} and obtain that $\lambda_{lim}^2 + \lambda_{lim}^{-2} - 2 = J_m$. The adopted Gent parameter was $J_m = 91$, corresponding to $\lambda_{lim} \approx 0.1037$. This asymptotic effect is seen for low values of d_0/L, with the transition occurring at $d_0/L \approx 0.13$. Actually, just below that threshold the electro-mechanical instability becomes less pronounced until it quickly disappears (the curve for $d_0/L = 0.12$ is monotonic). This is caused by the stretch limit preventing further material expansion.

Figure 4 shows all the fundamental paths starting from the natural configuration for both strain-energy functions and a pre-stressed neo-Hookean function represented on an electric displacement curve. The normalised electric displacement $\bar{D} = D_2/\sqrt{\mu\varepsilon}$ is plotted. The electric displacement curve does not depend on the geometry and as such encapsulates all fundamental paths. The black markers represent the expansion limit for each curve. As the d_0/L parameter decreases, a higher electric displacement can be reached before encountering the expansion limit. The Gent curve is steeper as it reaches asymptotically the extension limit of the polymer chains λ_{lim}.
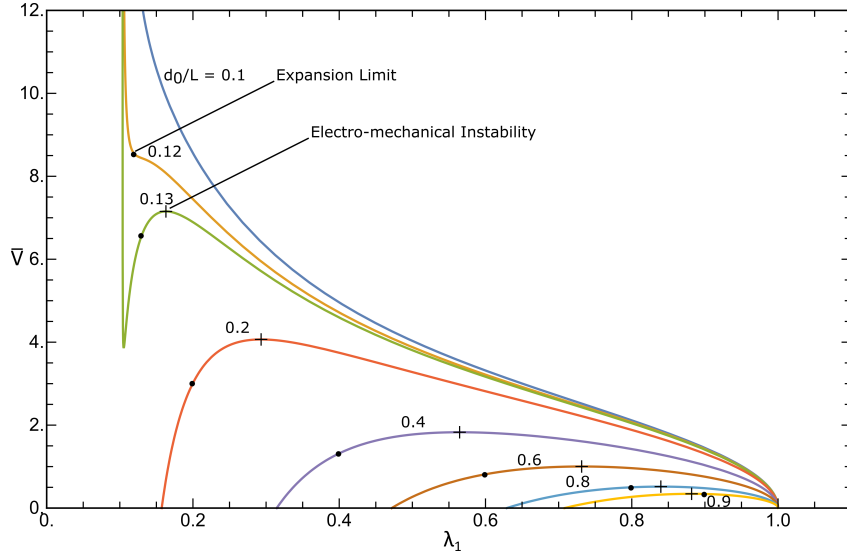
9

Figure 3: Fundamental loading paths for the actuated 'floating' elastomer in vacuum (Gent strain energy with $J_m = 91$, various values of the geometric ratio d_0/L are considered). λ_1 varies with the non-dimensional electric potential jump $\bar{V}$. Dots mark the expansion limit while crosses indicate the onset of the electro-mechanical instability.

3 Electro-elastic surface instability

In this section, we specialise the incremental theory to identify electro-elastic surface instabilities on a pre-stressed elastomer half-space under plane-strain conditions. We then introduce incremental boundary conditions suitable for the loading paths introduced in Section 2.4 A), B) and C). The numerical results, highlighting the onset of surface instability for the three cases are then discussed. The theory is further enriched by introducing the surface-coating theory, to take into account the effect of the stiffness of the electrode to the surface instability of a substrate, following the path described in Section 2.4 A).

3.1 Perfectly compliant electrode

The electro-elastic modelling framework is specialised to seek bifurcation with a possible presence of an external electric field normal to its boundary. The substrate is possibly pre-stressed along the x_1 direction ($\tau_{pre} \neq 0$) and is subjected to a plane incremental deformation. In turn, this means that the out-of-plane component of the displacement is null, i.e. $u_3 = 0$, and $\boldsymbol{u}$ depends only on coordinates x_1 and x_2, i.e. $u_i = u_i(x_1, x_2)$ ($i = 1, 2$). Similarly, it is also assumed that $\hat{D}_3 = 0$, $\hat{D}_i = \hat{D}_i(x_1, x_2)$ ($i = 1, 2$) and $\dot{p} = \dot{p}(x_1, x_2)$. By adopting the updated Lagrangian formulation, eqs. (2.20) can be
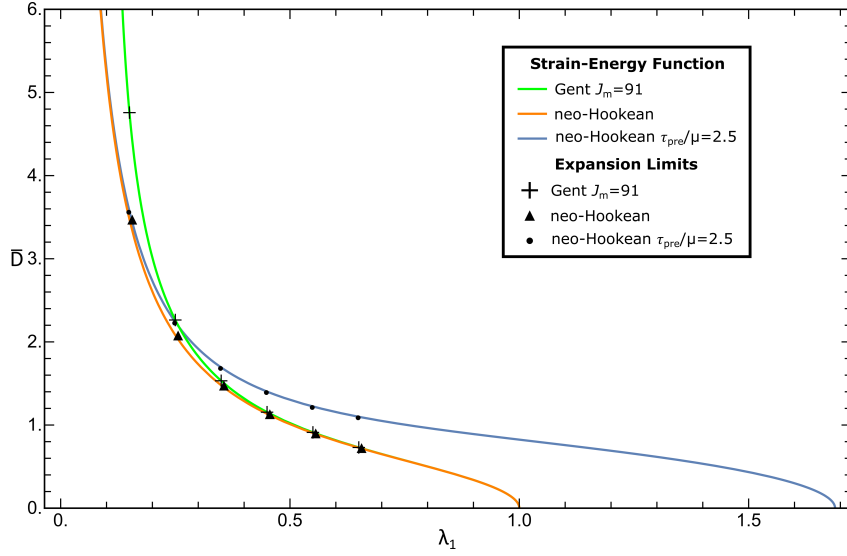
Figure 4: Fundamental loading paths for the actuated 'floating' elastomer in vacuum (for both neo-Hookean and Gent strain energies). λ_1 varies with the non-dimensional electric displacement $\bar{D}$. Black markers mark the expansion limit for each curve; ratio d_0/L is varied from 0.15 to 0.65 in increments of 0.10.

written in component as

$$\Sigma_{11,1} + \Sigma_{12,2} = 0, \qquad \Sigma_{21,1} + \Sigma_{22,2} = 0,$$
$$\hat{D}_{1,1} + \hat{D}_{2,2} = 0, \qquad \hat{E}_{1,2} - \hat{E}_{2,1} = 0, \tag{3.1}$$

where a comma represents partial differentiation. Field eqs. (3.1) are satisfied by a solution of the form (the domain is the half-space $x_2 \geq 0$)

$$u_i(x_1, x_2) = v_i(x_2)\exp(ikx_1),$$
$$\hat{D}_i(x_1, x_2) = \Delta_i(x_2)\exp(ikx_1),$$
$$\dot{p}(x_1, x_2) = q(x_2)\exp(ikx_1), \tag{3.2}$$

with k being the wave-number of the perturbation. We expect that the electro-elastic surface instability be independent of k. The incompressibility constraint $u_{1,1} + u_{2,2} = 0$ imposes to eqs. (3.2) that

$$ikv_1(x_2) + v_2'(x_2) = 0; \tag{3.3}$$

similarly, eq. $(3.1)_3$ dictates

$$ik\Delta_1(x_2) + \Delta_2'(x_2) = 0. \tag{3.4}$$

Bifurcation modes must decay deep in the half-space, as $x_2 \to \infty$, therefore an admissible general form of v_2, Δ_2 and q is

$$v_2(x_2) = U\exp(skx_2),$$
$$\Delta_2(x_2) = W\exp(skx_2),$$
$$q(x_2) = Q\exp(skx_2), \tag{3.5}$$

11

where $s < 0$. By substituting them into eqs. (3.2), we obtain a system of equations for the three unknowns U, W and Q. A non-trivial solution requires that the determinant of the coefficients vanishes, leading to a polynomial equation (of the 6th order) in s. However, the only admissible solutions are the three negative roots of s, namely $s_j < 0$ ($j = 1, 2, 3$). Therefore, the general expressions for the bifurcation fields are

$$v_2(x_2) = \sum_{j=1}^{3} U_j \exp(s_j k x_2),$$

$$\Delta_2(x_2) = \sum_{j=1}^{3} W_j \exp(s_j k x_2),$$

$$q(x_2) = \sum_{j=1}^{3} Q_j \exp(s_j k x_2). \tag{3.6}$$

The coefficients appearing in (3.6) are not independent and eqs. (3.2) can be employed to find their connection. In particular, Q_j and W_j can be expressed in terms of U_j ($j = 1, 2, 3$).

Incremental equations in vacuum. In some of the analysed problems, it is mandatory to deal with the external incremental fields in vacuum B^*, where Maxwell's equations hold for $\boldsymbol{D}^*$ and $\boldsymbol{E}^*$. In those cases, we assume the existence of an electric potential $\phi^*(x_1, x_2)$ that satisfies the Laplace's equation

$$\phi^*_{,11} + \phi^*_{,22} = 0. \tag{3.7}$$

A solution compatible with the decaying of effects as $x_2 \to -\infty$ is

$$\phi^*(x_1, x_2) = \phi_c \exp(k x_2) \exp(i k x_1), \tag{3.8}$$

where ϕ_c is the amplitude. It may be useful to recall that, as a function of ϕ^*, the incremental Maxwell stress tensor has the following non-zero components

$$\dot{T}^*_{11} = \dot{T}^*_{33} = -\dot{T}^*_{22} = \varepsilon_0 E_2^* \phi^*_{,2},$$
$$\dot{T}^*_{12} = \dot{T}^*_{21} = -\varepsilon_0 E_2^* \phi^*_{,1}. \tag{3.9}$$

Incremental boundary conditions and bifurcation equation. We recall eqs. (2.23), which are the incremental boundary conditions specialised for a discontinuity between the elastomer surface and an adjacent vacuum. For relevant practical applications, both the surface tractions and the surface charges are independent of deformation and as such $\boldsymbol{\dot{t}}^0 = \boldsymbol{0}$ and $\dot{\omega}^0 = 0$. On $x_2 = 0$, eq. (2.23)$_1$ reduces to the following scalar equations

$$\Sigma_{21} + T_{11}^* u_{2,1} + T_{21}^* u_{2,2} - \dot{T}^*_{21} = 0,$$
$$\Sigma_{22} + T_{22}^* u_{2,2} + T_{21}^* u_{2,1} - \dot{T}^*_{22} = 0. \tag{3.10}$$

Similarly, for eq. $(2.23)_2$ on $x_2 = 0$, it turns out

$$\hat{D}_2 + D_1^* u_{2,1} + D_2^* u_{2,2} - \dot{D}_2^* = 0,$$
$$\hat{E}_1 - E_1^* u_{1,1} - E_2^* u_{2,1} - \dot{E}_1^* = 0. \tag{3.11}$$

This provides a system of four homogeneous equations. For a non-trivial solution of the bifurcation problem, the determinant of the coefficients U_j ($j = 1, 2, 3$) and ϕ_c must vanish yielding the *bifurcation equation*. It is worth to mention that an alternative way to study bifurcation is to use the fields (3.6), (3.2) and (3.8) into the integral formulation obtained by Gei et al. [31] and applied by Siboni et al. [33]. The fields can also be adapted to be used in the Stroh formulation [34].

Specialised boundary conditions for the three electro-elastic problems. We adapt the general theory to the three fundamental loading paths introduced in Section 2.4 to study the onset of surface instabilities for each type of actuation. To solve our incremental equation system, eqs. (3.10) and (3.11), boundary conditions need to be specified for the three cases. Just as a reminder, for all three configurations we assume that the electric actuation is along the thickness of the elastomer, therefore

$$D_1^* = E_1^* = 0, \quad D_1 = E_1 = 0. \tag{3.12}$$

The elastomer may be subjected to a (current) pre-stress τ_{pre} along x_1. As such, the stress boundary conditions (2.1) specialise in

$$\tau_{22} = T_{22}^*, \quad \tau_{pre} = \tau_{11} - T_{11}^*. \tag{3.13}$$

In both cases detailed in Section 2.4 A) and B), there is no external electric field, namely

$$D_2^* = E_2^* = 0 \tag{3.14}$$

and, as a consequence, the Maxwell stress tensor vanishes, $\boldsymbol{T}^* = \boldsymbol{0}$. Conversely, for the elastomer 'floating' between electrodes (Section 2.4 C)), its components are obtained from eq. (2.3) and are given as follows,

$$\boldsymbol{T}^* = \begin{pmatrix} -\frac{(\varepsilon_0 E_1^*)^2}{2\varepsilon_0} & 0 \\ 0 & \frac{(\varepsilon_0 E_2^*)^2}{2\varepsilon_0} \end{pmatrix} = \begin{pmatrix} -\frac{(D_1^*)^2}{2\varepsilon_0} & 0 \\ 0 & \frac{(D_2^*)^2}{2\varepsilon_0} \end{pmatrix}. \tag{3.15}$$

Only two components are shown as we are dealing with a two-dimensional plane-strain case where the elastomer remains undeformed out-of-plane. The incremental boundary conditions may also be specialised to the three configurations. Likewise the finite-strain counterparts, for attached compliant electrodes and charged-controlled configurations, the incremental Maxwell stress tensor is null, $\dot{\boldsymbol{T}}^* = \boldsymbol{0}$. However, in the former case there are no fields in the vacuum and there the incremental electric field is also null, $\dot{D}_2^* = \dot{E}_2^* = 0$, differently from charge-controlled actuation where the charges are constrained on the surface of the substrate causing incremental fields to exist in the adjacent vacuum.
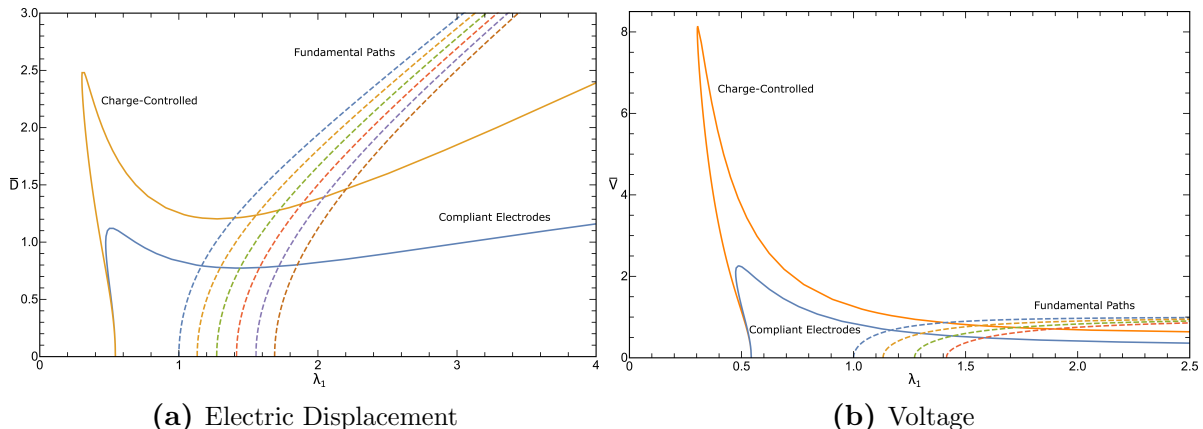
(a) Electric Displacement   **(b)** Voltage

Figure 5: Limit of the stability domains for a neo-Hookean substrate with either attached compliant electrodes or charge-controlled boundary condition. Dotted lines represent loading paths with τ_{pre}/μ starting from 0 with increments of 0.5. Figures (a) and (b) represent the same results, but with a different non-dimensional electric variable on the ordinate.

3.1.1 Results

The bifurcation equation was obtained and solutions sought for the three different electro-elastic actuation paths, introduced in Section 2.4, were plotted using the specialised boundary conditions in the previous section. In order to obtain the bifurcation equation, the expression of W_{elec} presented in eq. (2.14) was used to avoid double multiplicity of roots s occurring when the ideal dielectric strain-energy equation is adopted. We then verified that the limit $\bar{\gamma}_0$, $\bar{\gamma}_2 \to 0$, $\bar{\gamma}_1 \to 1$ converges.

Figure 5 shows the limit of the stability domains for the half-space with attached compliant electrodes and charge-controlled actuation in blue and orange, respectively. They are plotted together with the fundamental loading paths, shown by the dotted lines, obtained from eq. (2.28). The pre-stress τ_{pre}/μ is varied, starting from 0 to 2.5, increasing in increments of 0.5. In Fig. 5 (a) the normalised electric displacement $\bar{D}$ is reported in the ordinate, whereas in (b) the normalised voltage $\bar{V}$ is selected. For the attached compliant electrodes and charge-controlled configurations the voltage is normalised using the initial thickness as $\bar{V} = (\Phi/d_0)\sqrt{(\varepsilon/\mu)}$. Surface instabilities occur at lower values of the electric actuation over the whole domain for the finite deformation induced by attached compliant electrodes. This shows the stabilising effect from the presence of the incremental outer electric field, as $\dot{D}_2^*$ and $\dot{E}_2^*$ are not null for the charge-controlled actuation.

In both cases, the elastomer could theoretically reach high values of $\bar{D}$ or $\bar{V}$ by controlling the loading path to make the stable path to reach the local maxima evident in the bifurcation domains. This peak is more pronounced in the charge-controlled actuation compared to the attached compliant electrodes and can be seen even more marked when the voltage is represented allowing theoretically much higher voltages to be reached. Given the almost flat trend of the curves limiting the stability domains between $1 < \lambda < 2$, the pre-stress does not have much influence on the onset of sur-
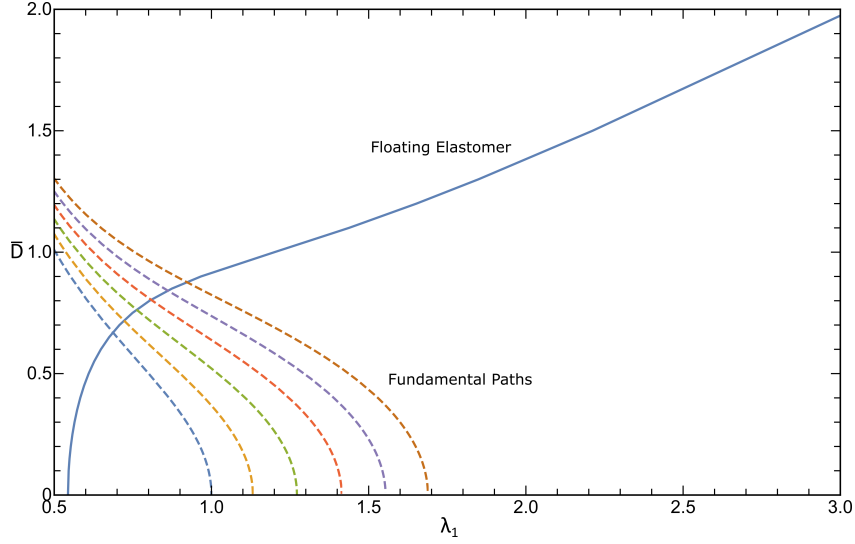
14

Figure 6: Limit of the stability domain for a neo-Hookean substrate actuated as a 'floating' elastomer in vacuum. Dotted lines represent loading paths with τ_{pre}/μ going from 0 to 2.5 in increments of 0.5. Actuation is represented by the non-dimensional electric displacement $\bar{D}$.

face instabilities. To highlight the magnitude of voltages at bifurcation, we consider an elastomer with thickness $d_0 = 700$ μm, and material parameters set as $\varepsilon = 4.68\,\varepsilon_0$ and $\mu = 100$ kPa, which model well PDMS/silicone-based dielectric elastomers [35]. Following the fundamental loading curve for $\tau_{pre} = 0$, we obtain that surface instability occurs at approximately 23.4 kV and 29.7 kV for compliant attached electrodes and charge-controlled configurations, respectively.

Figure 6 shows the stability domain for the 'floating' elastomer configuration plotted as a λ vs. $\bar{D}$ diagram. The electric displacement is instrumentally used, as it is independent of the aspect ratio d_0/L of the film, thus representing the critical states of all possible geometries. Again, the dotted lines show the fundamental loading path from eq. (2.33) with a pre-stress τ_{pre}/μ going from 0 to 2.5 in increments of 0.5. Differently from the previous cases, the bifurcation curve does not show a local maximum. Now a tensile pre-stress is more influential as it allows the elastomer to experience higher values of $\bar{D}$ in a stable configuration. Continuing the comparison with the two previous actuation methods, for the 'floating' elastomer case the surface instability occurs at a lower value of $\bar{D}$. Specific geometries for the specimen were then analysed using the non-dimensionalised voltage $\bar{V}$. Figure 7 shows two characteristic loading paths (in blue) combined with bifurcation curves (in orange) for two extreme values of d_0/L (the expansion limit is represented by a black dot along the curve). When the elastomer is very thick compared to the gap between the electrodes, as in Fig. 7 (b), the elastomer hits the expansion limit before the onset of surface instabilities. With low values d_0/L (Fig. 7 (a)), the elastomer expands a lot more and intersects the bifurcation curve before it reaches that limit, implying that surface instabilities are promoted by a thinner elastomers.
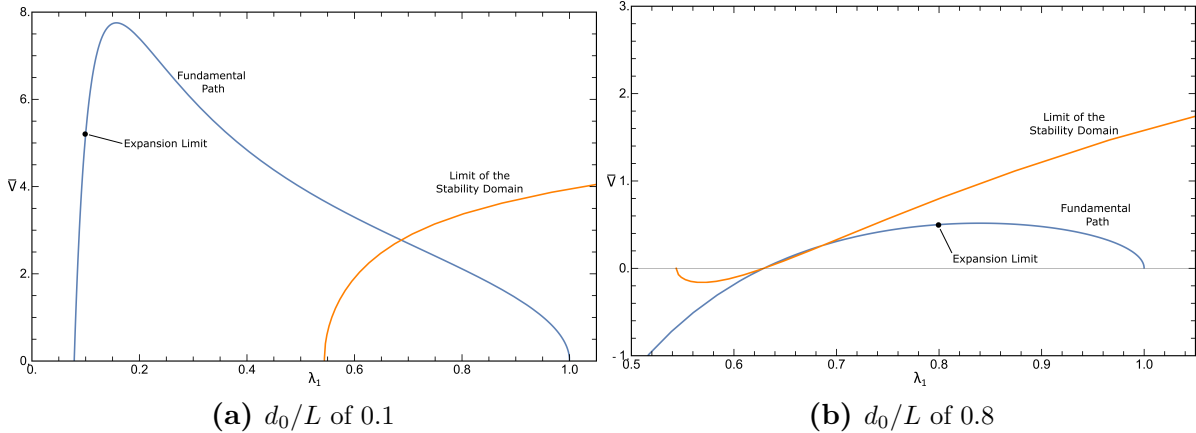
15

(a) d_0/L of 0.1
(b) d_0/L of 0.8

Figure 7: Fundamental path for a neo-Hookean substrate actuated as a 'floating' elastomer (blue) and the limit of the stability domain (orange) for $d_0/L = 0.1$ (a) and $d_0/L = 0.8$ (b). Dots mark the expansion limit in each case. λ_1 varies with the non-dimensional electric potential jump $\bar{V}$.

To better understand the characteristics of the surface instability, incremental fields at the onset of bifurcation were studied. The simple loading path with no pre-stress was chosen, at the point of intersection with the bifurcation curve. Coefficients U_j ($j = 1, 2, 3$) and ϕ_c were solved for the specific case. They were normalised such that the displacement u_2 at the surface was 5% of the wavelength of the deformation. Figure 8 displays the plot of this quantity into the thickness of the elastomer normalised with the wavelength $x_2 k/(2\pi)$ (k selected as a unitary value). reported curves show that the attached compliant electrodes and the charge-controlled cases exhibit a similar incremental deformation. They decay a lot faster into the thickness, within one wavelength, compared to the actuated 'floating' elastomer counterpart. In addition, in the latter mode, the elastomer exhibits a maximum expansion just under the surface before decaying. Figure 9 demonstrates how the boundary conditions influence the component parallel to the surface, of the normalised incremental electric field $\bar{E}_1 = \hat{E}_1/\sqrt{\mu/\varepsilon}$. Following our specialised incremental boundary conditions, as expected it can be noted that for the attached compliant electrodes (in orange) $\bar{E}_1$ is null, whereas that is not the case for the other two configurations. For the first analysed fundamental path, $\bar{E}_1$ increases significantly into the depth of the elastomer before decaying again. For the other two actuation cases this does not occur. The difference between the charged-controlled and floating configurations is that the former shows the longitudinal incremental electric field decaying slower even though it has a lower maximum value. This correlates to the incremental displacement field plots in Fig. 8.

3.2 Effect of the stiffness of the electrode

The effect of the stiffness of the electrode on surface instability can be analysed by using the theory of surface coating to obtain boundary conditions for the electro-elastic substrate. This follows the work done by Steigmann and Ogden [29, 30], who explored
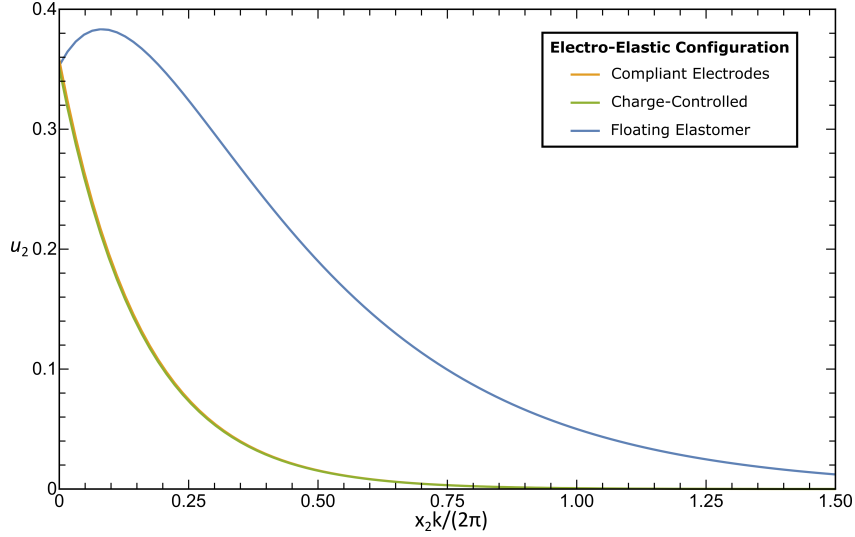
16

Figure 8: Incremental displacement u_2 into the elastomer thickness normalised with the wavelength $(x_2 k/(2\pi))$ for the three analysed electro-elastic problems.
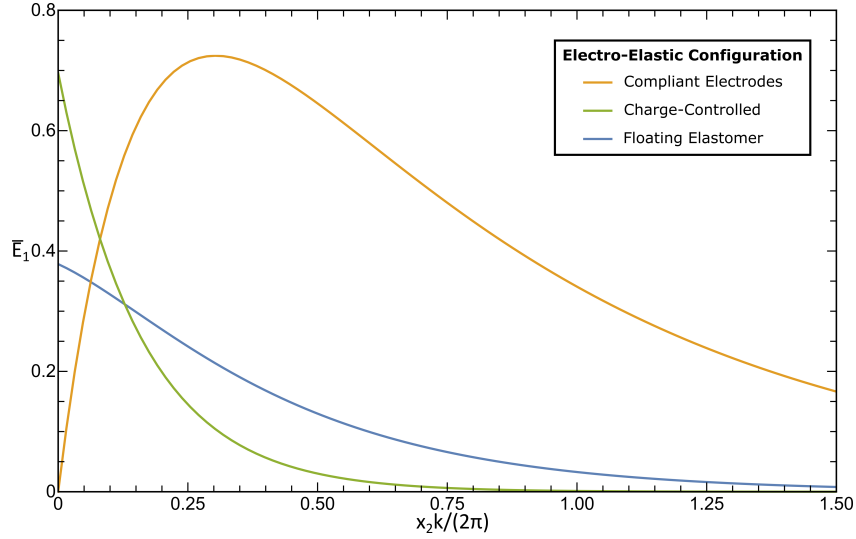

Figure 9: Normalised incremental longitudinal electric field $\bar{E}_1$ into the elastomer thickness normalised with the wavelength $(x_2 k/(2\pi))$ for the three analysed electro-elastic problems.

bifurcation of and wave propagation on an elastic half-space with a thin coating on its plane boundary. In this section, we recall the basic notions of the surface-coating theory suitable for incremental fields.

The electrode film is assumed to be fully compliant to the elastomer such that, in the pre-bifurcation state, the stretch λ is the same in both elements. As shown in Fig. 10, $\boldsymbol{\nu_1}(S)$ is the unit tangent to the surface that is described by an arc length S. Vectors $\boldsymbol{e}_1$ and $\boldsymbol{e}_2$ form the orthonormal unit basis associated with x_1^0 and x_2^0. The leftward unit normal is defined by $\boldsymbol{\nu_2}(S) = \boldsymbol{k} \times \boldsymbol{\nu_1}(S)$, where $\boldsymbol{k} = \boldsymbol{e}_1 \times \boldsymbol{e}_2$. If $\theta(S)$ is the counter-

clockwise angle between $\boldsymbol{\nu_1}$ and $\boldsymbol{e}_1$, differentiation with respect to S yields

$$\boldsymbol{\nu_1'}(S) = \kappa(S)\boldsymbol{\nu_2}(S), \quad \kappa(S) = \theta'(S), \tag{3.16}$$

where $()' = d/dS$ and $\kappa(S)$ is the nominal curvature of the film. The coating is characterised by the elastic strain energy per unit length $U(\Lambda, \kappa)$, where the first argument is the current axial stretch of the electrode. Axial force and bending moment can be obtained by partial differentiation, namely,

$$F = U_{,\Lambda} \quad \text{and} \quad M = U_{,\kappa}. \tag{3.17}$$

In addition to the axial component, the total force at a generic point of the surface has a normal component, say G, such that

$$\boldsymbol{f} = F\boldsymbol{\nu_1} + G\boldsymbol{\nu_2}. \tag{3.18}$$

G is not obtained by a constitutive equation as the thin film is assumed to have vanishing thickness: it is an unknown of the problem. Following [29, 30], linear momentum and moment-of-momentum balances for the film give the local equations

$$\boldsymbol{f}' = \boldsymbol{SN}, \quad M' + \Lambda G = 0, \tag{3.19}$$

being the latter the required condition to determine G.

We require incremental boundary conditions to add to our bifurcation problem. Therefore, we take the increment of the eqs. (3.19) and update them from S to current arc length s, given that $\Lambda = \mathrm{d}s/\mathrm{d}S$, yielding

$$\dot{\boldsymbol{f}}'(s) = \boldsymbol{\Sigma n}, \quad \dot{M}(s) + \Lambda^{-1}\dot{\Lambda}G + \dot{G} = 0. \tag{3.20}$$

The incremental counterpart of eq. (3.18) gives $\dot{\boldsymbol{f}} = \dot{F}\boldsymbol{\nu_1} + \dot{G}\boldsymbol{\nu_2} + F\dot{\boldsymbol{\nu_1}} + G\dot{\boldsymbol{\nu_2}}$, and by knowing that $\dot{\boldsymbol{\nu_1}} = \dot{\theta}\boldsymbol{\nu_2}$ and $\dot{\boldsymbol{\nu_2}} = -\dot{\theta}\boldsymbol{\nu_1}$, the following equation is achieved

$$\dot{\boldsymbol{f}} = (\dot{F} - G\dot{\theta})\boldsymbol{\nu_1} + (F\dot{\theta} + \dot{G})\boldsymbol{\nu_2}. \tag{3.21}$$

The expression for $\dot{\boldsymbol{f}}'$ can be obtained from eq. (3.21) once $\dot{G}$ and G are known. To solve the terms $\dot{G}$ and G, eqs. (3.20) and (3.19) are employed. The use of $\boldsymbol{\nu_1} = \theta'\boldsymbol{\nu_2} = \Lambda^{-1}\kappa\boldsymbol{\nu_2} = -\theta'\boldsymbol{\nu_1}$, $\boldsymbol{\nu_2'} = -\theta'\boldsymbol{\nu_1} = -\Lambda^{-1}\kappa\boldsymbol{\nu_1}$ and $\dot{\theta}' = \Lambda^{-1}\dot{\kappa}$ yields

$$\dot{\boldsymbol{f}}' = T\boldsymbol{\nu_1} + N\boldsymbol{\nu_2}, \tag{3.22}$$

where

$$T = \dot{F}' + \Lambda^{-1}\dot{\kappa}M' + M''\dot{\theta} - \Lambda^{-1}\kappa(F\dot{\theta} + M'\Lambda^{-1}\dot{\Lambda} - \dot{M}'),$$
$$N = \Lambda^{-1}\dot{\kappa}F + F'\dot{\theta} + \Lambda^{-1}M'(\dot{\Lambda}' - \Lambda^{-1}\Lambda'\dot{\Lambda}) + \Lambda^{-1}\dot{\Lambda}M'' - \dot{M}'' + \Lambda^{-1}\kappa(\dot{F} + M'\dot{\theta}). \tag{3.23}$$

The following kinematic expressions are needed to solve the incremental variables:

$$\dot{\Lambda} = \Lambda\boldsymbol{\nu_1} \cdot \boldsymbol{u}', \quad \dot{\kappa} = \Lambda\boldsymbol{\nu_2} \cdot \boldsymbol{u}'' - \kappa\boldsymbol{\nu_1} \cdot \boldsymbol{u}', \quad \dot{\theta} = \boldsymbol{\nu_2} \cdot \boldsymbol{u}', \tag{3.24}$$
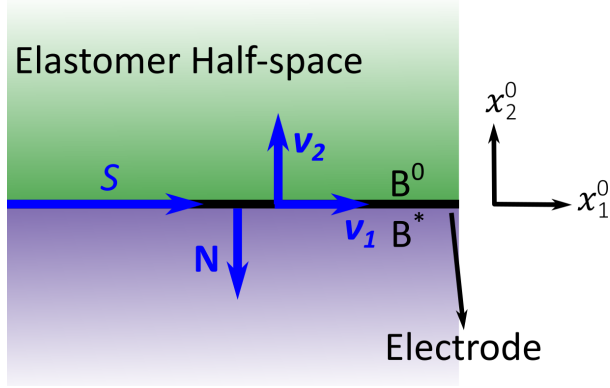
Figure 10: Sketch of the electro-elastic half-space in the reference configuration (B^0) coated by a 'stiff' electrode. B^* represents the surrounding vacuum.

where $\boldsymbol{u}$ is the incremental displacement field at the boundary of the half-space defined in previous sections.

The Cartesian coordinate system specific of our problem and indicated in Fig. 10 is aligned with the basis such that $\boldsymbol{\nu_1} = \boldsymbol{e}_1$, $\boldsymbol{\nu_2} = \boldsymbol{e}_2$, $\boldsymbol{n} = -\boldsymbol{e}_2$ and $\kappa = M' = G = 0$. We also specialise to the previously introduced dielectric body problem by noting that $\Lambda = \lambda$, as the electrode deforms with the elastomer homogeneously. Therefore, with the help of eqs. (3.24), we can simplify eqs. (3.23) and insert the results into eq. (3.20) to obtain our boundary conditions for the incremental problem, i.e.

$$\Sigma_{12} = -U_{\lambda\lambda}\lambda u_1'' - U_{\lambda\kappa}\lambda u_2''', \quad \Sigma_{22} = U_{\kappa\kappa}\lambda u_2'''' + U_{\kappa\lambda}\lambda u_1''' - U_\lambda u_2''. \tag{3.25}$$

A simple elastic strain-energy function for the electrodes can be chosen [30] as

$$U(\lambda, \kappa) = \frac{1}{2}m(\lambda - 1)^2 + \frac{1}{2}n\kappa^2, \tag{3.26}$$

which is an expression analogous to that of structural plates with stretching and bending. As such, it can be deduced that the parameters m and n may be interpreted as

$$m = \frac{E_c h}{1 - \nu_c^2}, \quad n = \frac{E_c h^3}{12(1 - \nu_c^2)}, \tag{3.27}$$

where E_c and ν_c are the Young's modulus and Poisson's ratio for the coating material, respectively, and h is the film thickness. Additional terms could be added to $U(\lambda, \kappa)$ to take residual stresses into account, but are assumed to be null in this investigation.

3.2.1 Effect of the stiffness of the electrode on surface instability

In this section we examine three different types of electrodes to show a range of materials that might be typically encountered, and obtain the bifurcation equation to analyse electro-elastic surface instabilities.

19

We recall eqs. (3.11) and (3.10) being the generic incremental boundary conditions for the elastomer. These conditions are specialised as previously described for the attached compliant electrodes case, which is the pertinent case when wanting to include electrode stiffness effects. To take the stiffness of the electrodes into account, we use the boundary conditions derived and given by eqs. (3.25), acting on the incremental stress terms. Using these new conditions and the strain-energy function for the electrode eq. (3.26), the bifurcation equation was obtained as previously described. It is important to note that the introduction of the electrode stiffness causes the bifurcation equation to be dependent on the wavenumber, in particular, due to the fourth-order derivative in eq. $(3.25)_2$, it is a quartic in k. We then expect a complex set of solutions depending on the wavenumber as also discussed by Ogden and Steigmann [30] and Gei [36]. It is worth to mention that we have verified our model by obtaining the elastic results presented in [30], where the electric field is absent.

Material properties for the electrodes are needed to obtain the material parameters m and n in eqs. (3.27), namely, Young's modulus and Poisson's ratio. The material properties m and n have dimensions of $length \times pressure$ and $length^3 \times pressure$, respectively. As such $(n/m)^{1/2}$ can be used as a length scale to normalise the wavenumber as $\bar{k} = k(n/m)^{1/2}$. To compare the three electrode materials, m and n are also normalised such that $\bar{m} = \bar{n} = (m/\mu)(m/n)^{1/2}$; in addition, they are assumed as incompressible. All the chosen materials may undergo large strains as they are highly stretchable and offer good conductivity.

The first material consists of a PDMS matrix combined with conductive materials such as graphene or carbon black. Typical values for Young's modulus is shown to be 0.9 MPa with an electrode thickness of $h = 30$ μm [37, 38], giving $m = 35.5$ Pa m, $n = 2.66 \times 10^{-9}$ Pa m^3 and $\bar{m} = 41.57$. The second material shares the matrix with the first one, but the reinforcement is composed of metal ions, such as gold or titanium, that are implanted into the PDMS matrix. Information on the manufacturing process and their material parameters were shown by Niklaus and Shea [39] and Shea [40], which measured a Young's modulus of 2 MPa and an electrode thickness of $h = 50$ nm. This provides $m = 0.13$ Pa m, $n = 2.74 \times 10^{-17}$ Pa m^3, and $\bar{m} = 91.17$. Alternative electrode materials are ionogels which consist of an ionic liquid immobilised in a polymer matrix. Material values were taken by Ji et al. [41], with a Young's modulus of 192 kPa and an electrode thickness of $h = 750$ nm, yielding $m = 0.19$ Pa m, $n = 8.88 \times 10^{-15}$ Pa m^3 and $\bar{m} = 8.75$.

As the bifurcation diagrams are similar for the three kinds of electrode, we analyse that of the graphene-implanted electrode (the first of the three) for which the dimensionless stiffness $\bar{m} = 41.57$ is the median one among the three materials. Figure 11 shows the bifurcation diagrams where λ is plotted against $\bar{k}$ for an increasing $\bar{D}$. For low values of the electric displacement, Fig. 11 (a) where $\bar{D} = 0.01$, there is only one solution of the bifurcation equation as for the uncoated half-space. The critical λ in this case is the maxima of the curve (i.e., $\bar{k} = 0.290$, $\lambda = 0.799$). It is of note that, as $\bar{k} \to 0$, the solution for negligible electrode stiffness (i.e., uncoated half-space) is obtained. For $\bar{D} > 0.773$, a new branch emerges (see Fig. 11 (b)). This provides two additional solutions at low
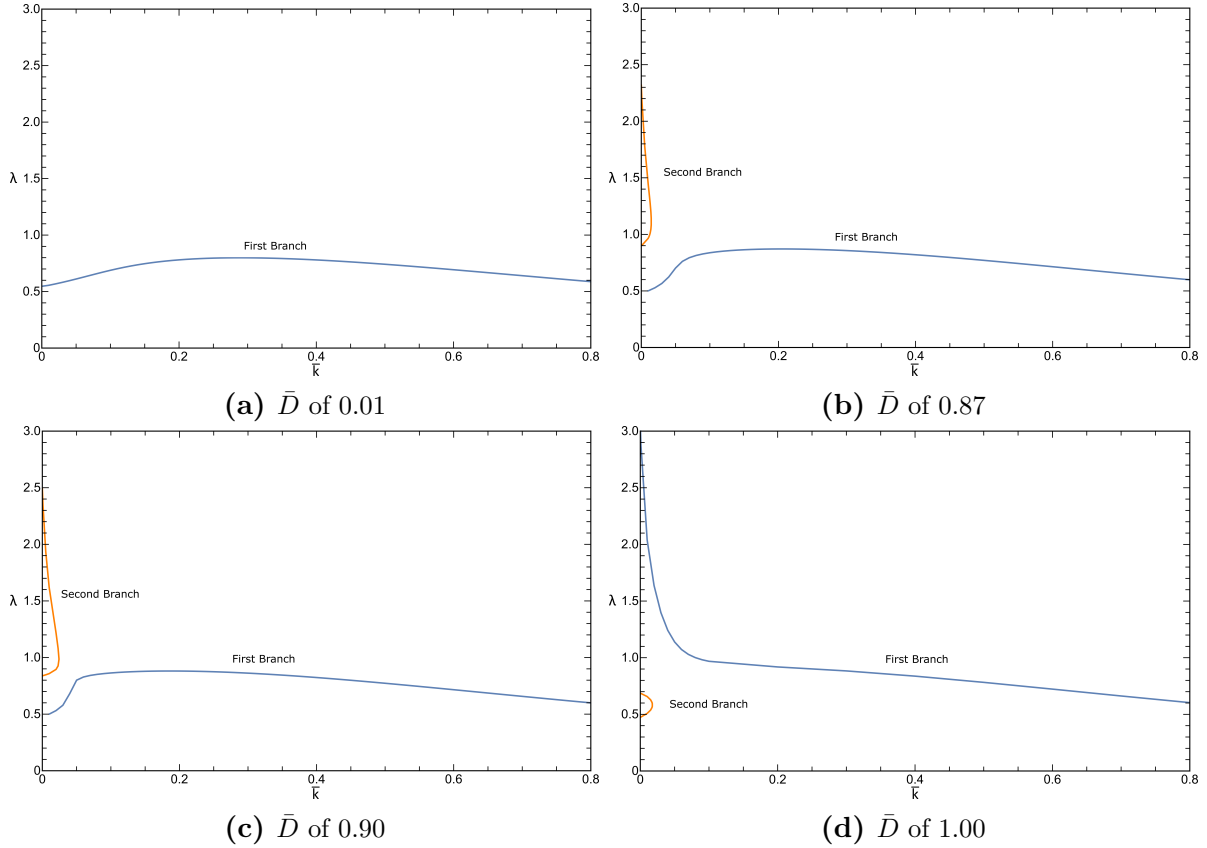
Figure 11: Bifurcation diagram for an actuated neo-Hookean elastomer coated with a 'stiff' electrode. The material parameters for a graphene implanted electrode were used, i.e. $\bar{m} = 41.57$. λ_1 is plotted against the normalised wavenumber $\bar{k}$ and various values of $\bar{D}$ are considered in the different plots. Blue and orange represent two different branches of the solution to the bifurcation equation.

$\bar{k}$. As $\bar{D}$ is increased further, the maxima from the first branch has a higher critical λ than the lowest solution of the new second branch (Fig. 11 (c)). This causes the overall bifurcation curve (displayed in Fig. 12) to have only one solution which is the one with the highest λ. The solution then switches form and the two branches merge into one (Fig. 11 (d)). The highest λ as $\bar{k} \to 0$ continues to be the dominant critical stretch as the maxima from the first branch disappears.

This instability curves for the various electrodes are plotted in Fig. 12. These are obtained checking carefully the critical λ (more than one solution may exist) on the bifurcation diagram analysed in Fig. 11 at a given $\bar{D}$. The curves pertain to ionogel (red), graphene-implanted (blue) and ion-implanted (green) electrodes, together with the solution where electrode stiffness is disregarded (orange) obtained in the previous subsection. Dotted lines represent loading paths of a dielectric elastomer (attached compliant electrode) with various states of pre-stress. Taking into account the stiffness of the electrodes causes the bifurcation curve to start at higher critical stretches for low $\bar{D}$, though always for $\lambda < 1$. The curves then go up much more linearly with a high slope until they reach
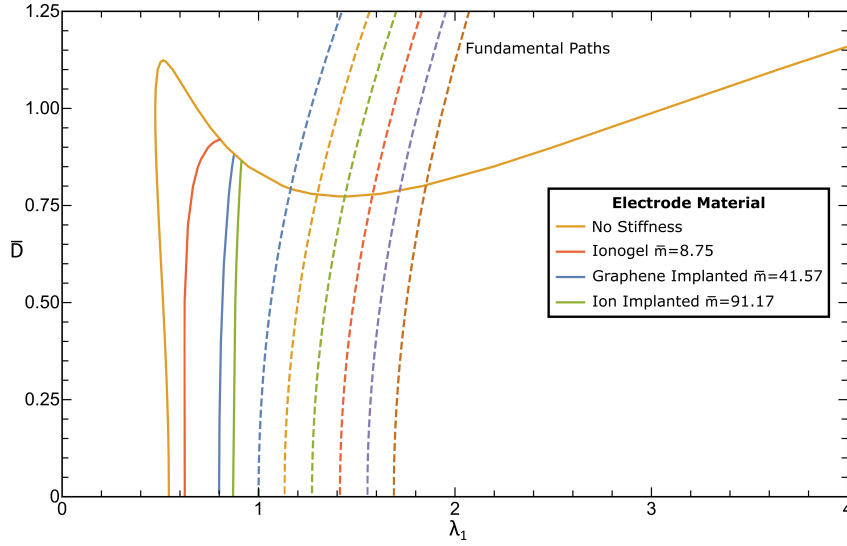
Figure 12: Limit of the stability domain for a neo-Hookean elastomer shown as various electrode materials with varying stiffness are assumed (varying $\bar{m}$). Dotted lines represent loading paths of a dielectric elastomer with τ_{pre}/μ going from 0 to 2.5 in increments of 0.5. Actuation is described by the non-dimensional electric displacement $\bar{D}$.

that for a fully compliant electrode, which then takes over. Compared to the uncoated case, the peak that was present vanishes in all the three cases. As $\bar{m}$ increases the bifurcation curve becomes more vertical and the critical lambda at $\bar{D} = 0$ also increases. However, following the fundamental paths considered in this investigation, this effect is not actually seen as the original curve takes over at a critical λ lower than the intersection of the fundamental paths.

To analyse the features of the bifurcation modes for the various branches described earlier, let us consider the parameter $\bar{D} = 0.85$, $\bar{k} = 0.001$, a case similar to that displayed in Fig. 11 (b). Again, the graphene-implanted electrode case is adopted ($\bar{m} = 41.57$). The three critical values of λ for the given $\bar{k}$ are equal to 0.482, 0.955 and 2.055. These values were used to calculate the eigensystem of the three coefficients (U_1, U_2, U_3, cf. eq. (3.6)), and the modes were normalised such that the incremental displacement $u_2 = 1$ at the surface of the half-space. The incremental displacement fields are displayed in Fig. 13. Functions u_2 and u_1 are plotted into the thickness of the elastomer x_2 normalised with the wavelength $2\pi/k$. The orange and green curves correspond to the solutions appearing only at a higher $\bar{D}$ corresponding to the orange branch in Fig. 11 (b), and are similar in nature. The blue curve, corresponding to the first branch with the lowest λ_{crit}, has a peak just inside the surface for the displacement u_2 and an inversion in u_1. In general, the two solutions from the second branch are more localised to the surface of the half-space, a findings similar to those observed in [30, 36] in analogous purely-elastic problems. This is also the case for the normalised transverse component of the incremental electric field, $\bar{E}_2$ in Fig. 14. For the electric fields, the general shape of the curve is very similar. However, with lower λ_{crit} values, the incremental electric field is much higher (over five
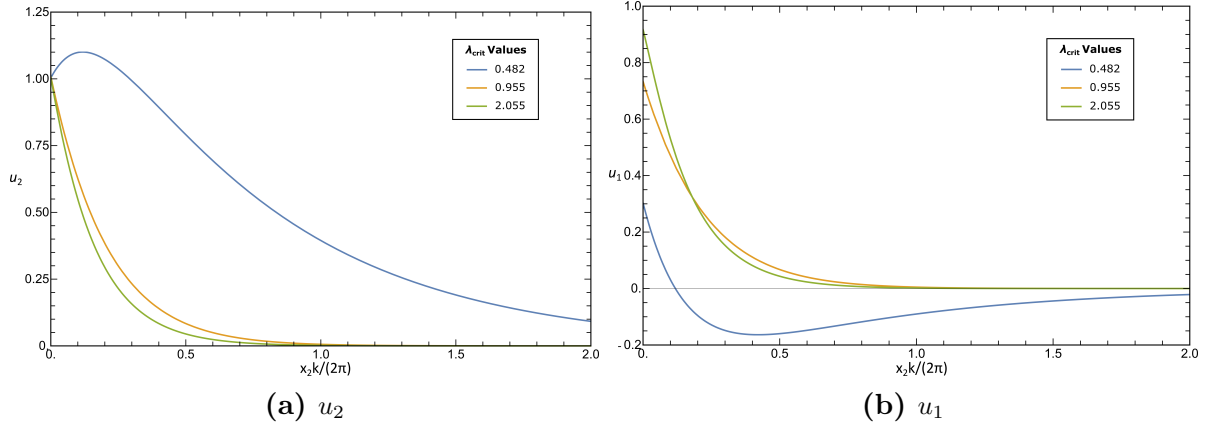
Figure 13: Incremental displacement fields u_2 and u_1, into the thickness x_2 of a neo-Hookean elastomer, normalised with the wavelength $2\pi/k$. The actuation case is that of an attached compliant electrodes with the stiffness taken into account. The material parameters for a graphene implanted electrodes was used with $\bar{m} = 41.57$. Curves represent the three solutions when $\bar{k} = 0.001$ and $\bar{D} = 0.85$, with varying λ_{crit} values.
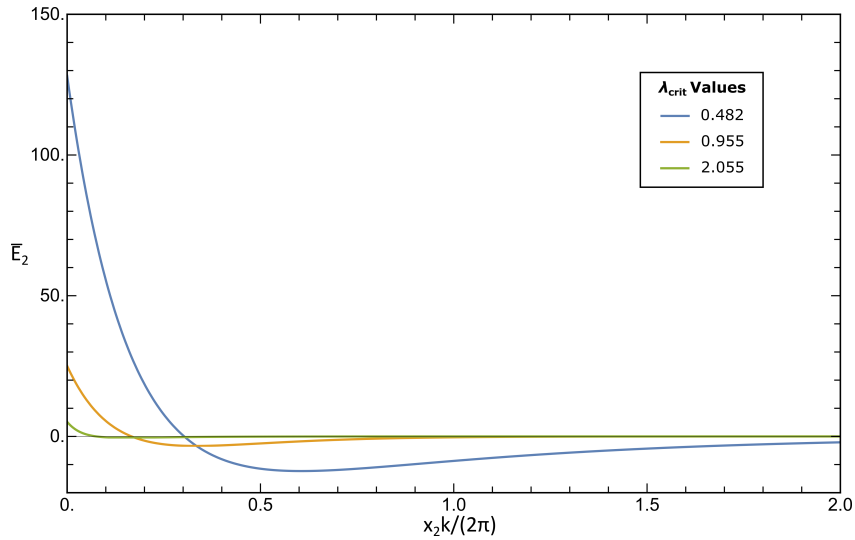

Figure 14: The normalised transverse incremental electric field $\hat{E}_2$, is shown into the thickness x_2 of a neo-Hookean elastomer, normalised with the wavelength $2\pi/k$. The actuation case is that of an attached compliant electrodes with the stiffness taken into account. The material parameters for a graphene implanted electrodes was used with $\bar{m} = 41.57$. Curves represent the solutions when $\bar{k} = 0.001$ and $\bar{D} = 0.85$, with varying λ_{crit} values.

times more) meaning an instability mode where the electric field plays a bigger role. It is also interesting to note that with the largest solution $\lambda_{crit} = 2.055$ there is a difference in the component $\bar{E}_1$ that distinguishes it from the other two solutions. While they all start off as $\bar{E}_1 = 0$ on the surface due to the electric boundary conditions, for this particular solution there is a peak just inside the thickness of the elastomer of a value around 10% the maximum $\bar{E}_2$. For the other solutions $\bar{E}_1$ is of several order of magnitudes lower.

(a) λ_{crit} of 0.482   **(b)** λ_{crit} of 0.955   **(c)** λ_{crit} of 2.055
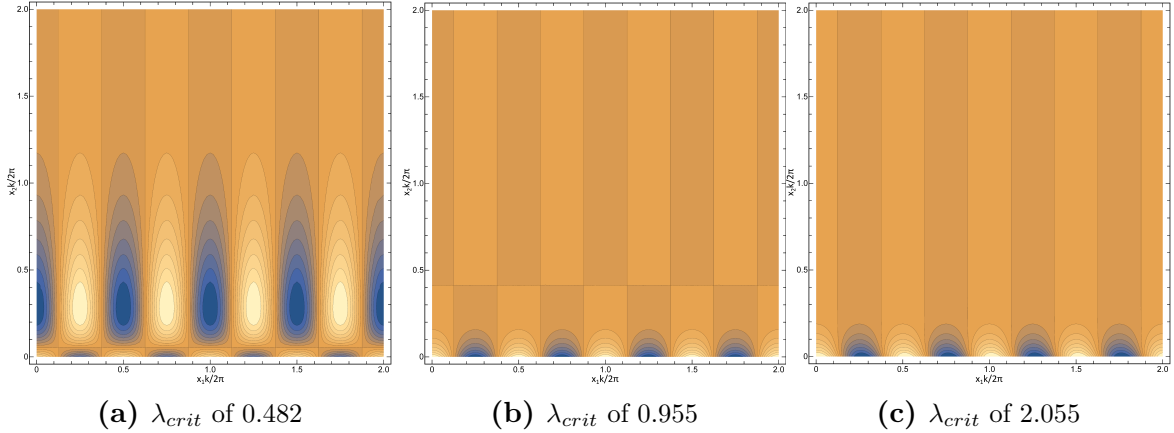
Figure 15: Contour plots of the incremental von Mises stress at the onset of instability for a neo-Hookean elastomer with a stiff electrode ($\bar{m} = 41.57$). The domain has been normalised with the wavelength $2\pi/k$. The three solutions correspond to $\bar{k} = 0.001$ when $\bar{D} = 0.85$, with varying values of λ_{crit} plotted separately.

We define the incremental von Mises stress as

$$\Sigma_v = \sqrt{\frac{1}{2}\left[(\Sigma_{11} - \Sigma_{22})^2 + (\Sigma_{22} - \Sigma_{33})^2 + (\Sigma_{33} - \Sigma_{11})^2\right] + 3(\Sigma_{12}^2 + \Sigma_{23}^2 + \Sigma_{31}^2)}. \quad (3.28)$$

In Fig. 15, the contour plots of incremental von Mises stress are plotted for the three values λ_{crit}. Here again we can see the big difference in decay into the thickness of the half-space with a lower λ_{crit}. It can also be observed that in Fig. 15 (a) there is a big inversion just inside the thickness of the elastomer implying an instability mode that has large varying stresses just under the surface. In Fig. 15 (b) the inversion is still present, but it appears when the incremental stress has already decayed and is almost null whereas in Fig. 15 (c) the plotted quantity decays monotonically with depth.

4   Conclusions

In coupled mechanics, the investigation of surface instability is an important step toward the complete understanding of the type of bifurcations occurring in a homogeneous body when subjected to external stimuli. In this paper we address plane-strain electro-elastic surface instability and, in particular, we aim at assessing the effect of the stiffness of electrodes on the stability domain.

To reach our goal, we introduce three ways to actuate an elastomer device (possibly pre-stressed), namely, actuation by means of (i) attached compliant electrodes, (ii) sprayed charges onto the opposite surfaces and (iii) fixed electrodes between which the device 'floats' in vacuum and expands transversally. The third mode is analysed in detailed with reference to the occurrence of the electro-mechanical instability and the expansion limit.

Surface instability is then tackled for the three actuation modes by specialising the relevant incremental theory where linearised fields are superimposed on the finite-strain path. The stability domains are obtained in the plane 'longitudinal stretch–dielectric displacement (or voltage jump)'. A first conclusion is that among the three modes, the instability is more sensible to pre-stress for specimens in the 'floating' configuration, while a half-space deformed by sprayed charges is more stable than the same actuated by voltage.

Surface-coating model can be profitably adopted to investigate the effects of electrodes on surface instability. Electrodes composed of three different materials are considered afterwards in the paper as employed in various applications. Their implementation in the model considerably changes the stability domain that is significantly reduced when the half-space contracts (longitudinal stretch less than one). New bifurcation modes come into play in this enriched approach and each one has been studied and characterised by analysing various incremental fields obtained solving the eigensystem governing the problem.

References

[1] Kofod, G., Wirges, W., 2007, Energy minimization for self-organized structure formation and actuation. *Appl. Phys. Lett.*, 90, 081916.

[2] Shintake, J., Cacucciolo, V., Shea, H., Floreano, D., 2018, Soft Biomimetic Fish Robot Made of Dielectric Elastomer Actuators. *Soft Rob.*, 5, pp. 466-474.

[3] Calabrese, L., Berardo, A., De Rossi, D., Gei, M., Pugno, N.M., Fantoni, G., 2019, A soft robot structure with limbless resonant, stick and slip locomotion. *Smart Mater. Struct.*, 28, 104005.

[4] Dubois, P., Rosset, S., Niklaus, M., Dadras, M., Shea, H., 2008, Voltage Control of the Resonance Frequency of Dielectric Electroactive Polymer (DEAP) Membranes. *AJ. Microelectromech. Syst.*, 17, pp. 1072-1081.

[5] Anderson, I.A., Gisby, T.A., McKay, T.G., O'Brien, B.M., Calius, E.P., 2012, Multi-functional dielectric elastomer artificial muscles for soft and smart machines. *J. Appl. Phys.*, 112, 041101.

[6] Cao, C., Burgess, S., Conn, A.T., 2019, Toward a Dielectric Elastomer Resonator Driven Flapping Wing Micro Air Vehicle. *Front. Robot. AI*, 5, pp. 137.

[7] Chiang, C., Lin, C.K., Ju, M., 2007, An implantable capacitive pressure sensor for biomedical applications. *Sens. Actuators, A*, 134, pp. 382-388.

[8] Carpi, F., Frediani, G., Gerboni, C., Germignani, J., De Rossi, D., 2014, Enabling variable-stiffness hand rehabilitation orthoses with dielectric elastomer transducers. *Med. Eng. Phys.*, 36, pp.205-211.

[9] Calabrese, L., Frediani, G., Gei, M., De Rossi, D., Carpi, F., 2018, Active compression bandage made of dielectric elastomers. *IEEE ASME Trans. Mechatron.*, 23, pp. 2328-2337.

[10] McKay, T.G., O'Brien, B.M., Calius, E.P., Anderson, I.A., 2011, Soft generators using dielectric elastomers. *Appl. Phys. Lett.*, 98, 142903.

[11] Kornbluh, R.D., Pelrine, R., Prahlad, H., Wong-Foy, A., McCoy, B., Kim, S., Eckerle, J., Low, T., 2011, From boots to buoys: promises and challenges of dielectric elastomer energy harvesting. *SPIE Proc.*, 7976, 797605.

[12] Bortot, E., Denzer, R., Menzel, A., Gei, M., 2014, Analysis of a viscous soft dielectric elastomer generator operating in an electric circuit. *Int. J. Solids Struct.*, 78-79, pp. 205-215.

[13] Moretti, G., Rosati Papini, G.P., Daniele, L., Forehand, D., Ingram, D., Vertechy, R., Fontana, M., 2019, Modelling and testing of a wave energy converter based on dielectric elastomer generators. *Proc. R. Soc. A*, 475, 20180566.

[14] Lu, T., Ma, C., Wang, T., 2020, Mechanics of dielectric elastomer structures: A review. *Extreme Mech. Lett.*, 38, 100752.

[15] Pelrine, R., Kornbluh, R.D., Joseph, J., 1998, Electrostriction of polymer dielectrics with compliant electrodes as a means of actuation. *Sens. Actuators, A*, 64, pp. 77-85.

[16] Röntgen, W.C., 1880, Ueber die durch Electricität bewirkten Form—und Volumenänderungen von dielectrischen Körpern. *Appl. Phys. Lett.*, 94, 262902.

[17] Keplinger, C., Kaltenbrunner, M., Nikita, A., Bauer, S., 2010, Röntgen's electrode-free elastomer actuators without electromechanical pull-in instability. *PNAS*, 107, pp. 4505–4510.

[18] Díaz-Calleja, R., Sanchis, M.J., Riande, E., 2009, Effect of an electric field on the bifurcation of a biaxially stretched incompressible slab rubber. *Eur. Phys. J. E*, 30, pp. 417-426.

[19] Kofod, G., Sommer-Larsen, P., Kornbluh, R.D., Pelrine, R., 2003, Actuation Response of Polyacrylate Dielectric Elastomers. *J. Intell. Mater. Syst. Struct.*, 14, pp. 787–793.

[20] Gatti, D., Haus, H., Matysek, M., Frohnapfel, B., Tropea, C., Schlaak, H.F., 2014, The dielectric breakdown limit of silicone dielectric elastomer actuators. *Appl. Phys. Lett.*, 104, 052905.

[21] Zhao, X., Suo, Z., 2007, Method to analyze electromechanical stability of dielectric elastomers. *Appl. Phys. Lett.*, 91, 061921.

[22] Bertoldi, K., Gei, M., 2011, Instability in multilayered soft dielectrics. *J. Mech. Phys. Solids*, 59, pp. 18-42.

[23] Zurlo, G., Destrade, M., DeTommasi, D., Puglisi, G., 2017, Catastrophic thinning of dielectric elastomers. *Phys. Rev. Lett.*, 118, 078001.

[24] Chen, L., Yang, X., Wang, B., Dayal, K., Sharma, P., 2017, The interplay between symmetry-breaking and symmetry-preserving bifurcations in soft dielectric films and the emergence of giant electro-actuation. *Extreme Mech. Lett.*, 43, 101151.

[25] Fu, Y., Dorfmann, L., Xie, Y., 2018, Localized necking of a dielectric membrane. *Extreme Mech. Lett.*, 21, pp. 44-48.

[26] Dorfmann, L., Ogden, R.W., 2019, Instabilities of soft dielectrics. *Philos. Trans. R. Soc. A*, 377, 20180077.

[27] Dorfmann, L. and Ogden, R.W., 2010, Nonlinear electroelastostatics: Incremental equations and stability. *Int. J. Eng. Sci.*, 48, pp. 1-14.

[28] Murdoch, A.I., 1976, The propagation of surface waves in bodies with material boundaries. *J. Mech. Phys. Solids*, 24, pp. 137–146.

[29] Steigmann, D.J., Ogden, R.W., 1999, Elastic surface-substrate interactions. *Proc. R. Soc. A*, 455, pp. 437-474.

[30] Ogden, R.W., Steigmann, D.J., 2002, Plane strain dynamics of elastic solids with intrinsic boundary elasticity, with application to surface wave propagation. *J. Mech. Phys. Solids*, 50, pp. 1869-1896.

[31] Gei, M., Colonnelli, S., Springhetti, R., 2014, The role of electrostriction on the stability of dielectric elastomer actuators. *Int. J. Solids Struct.*, 51, pp. 848-860.

[32] Su, Y., Chen, W., Dorfmann, L., Destrade, M., 2020, The effect of an exterior electric field on the instability of dielectric plates. *Proc. R. Soc. A*, 476, 20200267.

[33] Siboni, H.M., Avazmohammadi, R., Ponte Castañeda, P., 2014, Electromechanical instabilities in fiber-constrained, dielectric-elastomer composites subjected to all-around dead-loading. *Math. Mech. Solids*, 20, pp. 729-759.

[34] Edmondson, R.T., Fu, Y.B., 2009, Stroh formulation for a generally constrained and pre-stressed elastic material. *Int. J. Non-linear Mech.*, 44, pp. 530-537.

[35] Wissler, M., Mazza, E., 2007, Electromechanical coupling in dielectric elastomer actuators. *Sens. Actuators A*, 138, pp. 384-393.

[36] Gei, M., 2008, Elastic waves guided by a material interface. *Eur. J. Mech. A. Solids*, 27, pp. 328–345.

[37] Quinsaat, J.E.Q., Burda, I., Krämer, R., Häfliger, D., Nüesch, F.A., Dascalu, M., Opris, D.M., 2019, Conductive silicone elastomers electrodes processable by screen printing. *Sci. Rep.*, 9, 13331.

[38] Kujawski, M., Pearse, J. and Smela, E., 2010, PDMS/graphite stretchable electrodes for dielectric elastomer actuators. *Proc. SPIE, Electroactive Polymer Actuators and Devices (EAPAD)*, 7642, 76420R.

[39] Niklaus, M., Shea, H.R., 2011, Electrical conductivity and Young's modulus of flexible nanocomposites made by metal-ion implantation of polydimethylsiloxane: The relationship between nanostructure and macroscopic properties. *Acta Mater.*, 59, pp. 830-840.

[40] Shea, H.R., 2011, Miniaturized EAPs with compliant electrodes fabricated by ion implantation. *EAPAD 2011*, 7976, 79760R.

[41] Ji, X., Rosset, S., Shea, H.R., 2016, Soft tunable diffractive optics with multifunctional transparent electrodes enabling integrated actuation. *Appl. Phys. Lett.*, 109, 191901.